WIND TUNNEL TEST ON THE GALLOPING INSTABILITY OF A BRIDGE DECK WITH OPEN CROSS SECTION

Cong Chen, M.Sc.
TU - Braunschweig
Institut für Stahlbau
Beethovenstr. 51, Braunschweig
c.chen@stahlbau.tu-bs.de

Dr. Claudio Mannini
University of Florence
CRIACIV/DICEA
Via S. Marta, 3, Florence, Italy
claudio.mannini@unifi.it

Prof. Dr. Gianni Bartoli
University of Florence
CRIACIV/DICEA
Via S. Marta, 3, Florence, Italy
gianni.bartoli@unifi.it

Prof. Dr. Klaus Thiele
TU - Braunschweig
Institut für Stahlbau
Beethovenstr. 51, Braunschweig
k.thiele@stahlbau.tu-bs.de

ABSTRACT

The galloping instability was experimentally investigated for a bridge deck with open trapezoidal cross section, representing a typical cross section type during the construction phase of steel-concrete composite bridge girders. In smooth flow, unsteady galloping due to a strong interaction with vortex-induced vibration was observed for this bridged deck around a wind angle of attack of 4°, being the actual galloping onset fixed at the Kármán-vortex-resonance wind speed when the Scruton number is not higher than 70. This interaction was not encountered at the null wind angle of attack. Aerodynamic force measurements on stationary model indicated that the most evident difference between the two cases is the magnitude of the vortex shedding force, which is much lower for a null angle of attack. First results in turbulent flow with an intensity from 8.7% to 13.9% were also reported.

KURZFASSUNG

In diesem Beitrag wird eine experimentelle Untersuchung zu Galopping für einen offenen Trapezquerschnitt vorgestellt. Offene Querschnitte repräsentieren Stahlbetonverbund-Brückenträger während der Bauphase. In laminarer Strömung wurde eine starke Wechselwirkung zwischen wirbelinduzierter Vibration und Galopping für diesen Querschnitt um einen Windangriffswinkel von 4° beobachtet. Dabei entsprach die Windgeschwindigkeit der Kármán - Wirbelresonanz und die Scrutonzahl war nicht höher als 70. Diese Wechselwirkung war bei dem Nullwindwinkel nicht zu beobachten. Aerodynamische Kraftmessungen an stationären Modellen zeigten, dass ein wesentlicher Unterschied zwischen den beiden Windangriffswinkeln die Größe der Wirbelablösekraft ist, die für einen Nullanstellwinkel viel geringer ist. Erste Ergebnisse mit turbulenter Strömung der Intensität 8.7% bis 13.9% werden ebenfalls dargestellt.

1. Introduction

Across-wind galloping is an aeroelastic instability typical of slender structures with special cross sections, like square or D shape. Its onset and post-critical behavior can be well captured by the quasi-steady (QS) theory if a high reduced wind speed is ensured [1]. Otherwise, the unsteady effects of shed vortices and fluid memory become non-negligible and both QS galloping and vortex induced vibration (VIV) theories fail to explain the peculiar phenomena observed during wind tunnel tests [2]. In particular, the combined interference of galloping and VIV is able to promote an unrestricted oscillation starting at the Kármán-vortex resonance wind speed (U_r), instead of at the critical galloping wind speed (U_g) predicted by QS theory. In some other cases, the actual galloping onset was reported to occur earlier than U_g, although the VIV and galloping phenomena can already be observed separately. The mass - damping parameter Scruton number (Sc) is well accepted as one of the key parameters in controlling such an oscillation in airflow. Considering the dependence of galloping onset and post-onset behavior on the Scruton number, Mannini [3] classified this typical unsteady galloping into 3 groups namely i) full interference ii) partial interference and iii) low interference, based on the experimental results of a 3:2 rectangular cylinder in a smooth flow. On the other hand, a high Sc number is usually required to observe a so-called QS galloping in wind tunnel tests.

The previously discussed unsteady-galloping is not only physically interesting but also of great importance to some slender light-weight and low-damped structures. It implies that the quasi-steady theory which was adopted by many design standards, e.g. EN 1991-1-4 [4], may provide a prediction of galloping onset that stands not on the safe side, as mentioned also by Hansen [5]. In particular, this problem can be potentially encountered in the modern bridge-launching of the steel-concrete composite box girder. In the procedures of this method, the sole steel box is normally launched first due to its comparably lighter weight, prior to the construction of the concrete deck. However, these steel boxes could probably feature a much bluffer shape than the entire bridge cross section and usually are low-damped. These characteristics make the whole structural system more sensitive to wind exciting in the critical launching phase. It is worth giving here the example of the Aftetal Bridge (Germany) which falls in such a situation [6]. And its first 120m girder featuring an open cross section was finally covered with close-form wind claddings to eliminate the risk of transverse galloping during the launching process.

Due to the implication of a low Scruton number in this situation, unsteady galloping is probably a potential threat that should be seriously treated. A bridge deck model based on the prototype of Aftetal bridge but slightly modified was realized to conduct a wind tunnel investigation. It is worth mentioning that such a profile is quite typical during the bridge construction phase but limited attention has been paid so far to its aeroelastic stability. A rectangular cylinder model with the same general side ratio was also prepared as a reference. Turbulent flow was generated by means of grid to check its effect on the unsteady galloping instability of this bridge deck.

2. Wind tunnel tests

2.1 Wind tunnel facility and sectional models

The tests were carried out in the boundary layer wind tunnel at the Institute of Steel Structures of Technische Universität Braunschweig, Germany. It is a suction Eiffel-type facility with a rectangular test cross section of 1.4 m wide ×1.2 m high. The flow speed is continuously variable up to 25 m/s with a free-stream turbulence intensity about 1%. The ambient temperature, humidity and atmospheric pressure were monitored by a digital micro-manometer, to calculate the air density ρ.

Figure 1 shows the aluminum bridge deck model and the details of the cross section. It has a general side ratio $b/d = 2.0$ and a length $l_e = 1300$ mm between two 480 mm×240 mm×5 mm end-plates. The windward and leeward face both incline 15°. The bottom corners were purposely sharpened by two-component epoxy adhesive. The model's spatial stiffness was enhanced by the hollow ribs inside. An aluminum connecting tube was set to the centroid of the cross section at each end of the model. The mass of this model is 1.75 kg. The rectangular cylinder model is 1290 mm long, 120 mm wide and 60 mm deep and equipped with end-plates of the same size as the bridge model. Its aerodynamic shape was achieved by 5 mm thick balsawood plates, polished with sandpaper and protected with acrylic varnish. An aluminum square tube inside provides a suitable stiffness.

The wind tunnel blockage ratio was 5%, defined here as the ratio of model depth to wind tunnel height, and no blockage correction was considered for the test results. The mean wind speed in the wind tunnel was monitored by a Prandtl tube. Flow maps were prepared prior to the installation of the model to obtain more precise estimates of the wind speed U at the location of the model.

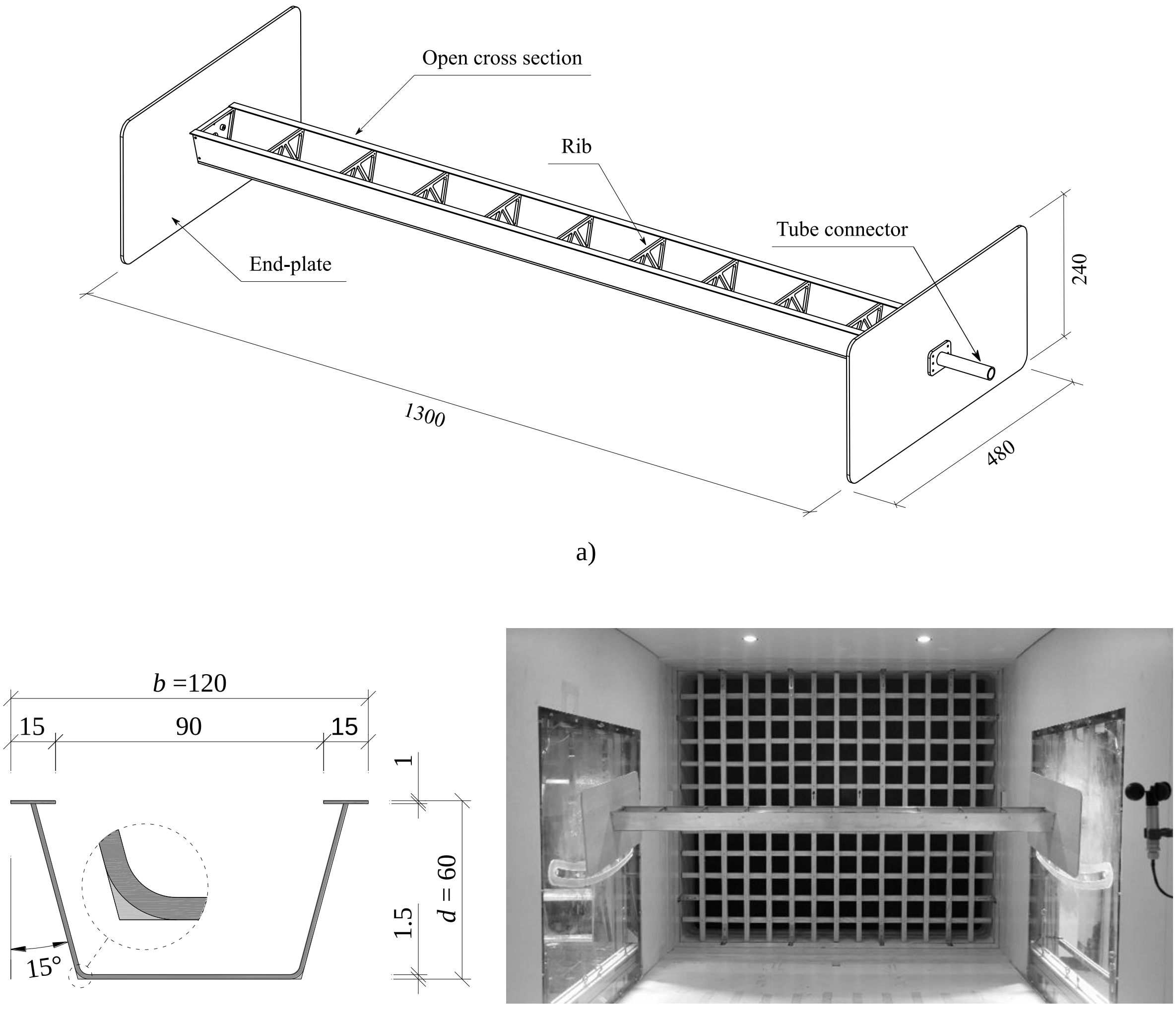

a)

b)

c)

Figure 1. a) sketch of the bridge deck model, b) dimension of the open cross section and c) photo of the bridge deck model mounted in wind tunnel with existence of turbulent grid windward (dimension in mm).

2.2 Test setup

The static setup consisted of three strain-gauge load cells (type HBM S2M), steel connecting rods and an aluminum block on each side of the wind tunnel, as shown in Figure 2. Each load cell was axially loaded due to the presence of two plate-shaped appendices in the connecting rod working as hinged connections. The wind tunnel model was rigidly connected to the aluminum blocks through three screws. Data acquisition was performed with a strain/bridge input module (type NI PXIe-4330) at a sampling frequency of 1000 Hz. The flow incidence of the models was manually adjusted with an electronic inclinometer (type SPI-TRONIC Pro 3600) with an accuracy of 0.05°.

The aeroelastic setup was composed by eight coil springs suspending the sectional models from outside the wind tunnel, with the horizontal motion restricted by two set of anti-drag cables. Two specially designed aluminum bars were used to link the wind tunnel model to the springs. The connection between the springs and the hooks of the bars was improved by means of nylon cables to avoid possible friction. The dynamic response of the model was measured by two laser displacement sensors (type WayCon LAS-T5-250-10V) on each side of the wind tunnel. Data were recorded at a sampling frequency of 1000 Hz with NI PXI-6284 module, a high-accuracy multifunction M Series module optimized for 18-bit analog input accuracy. Additional damping was introduced into the dynamic system by means of electromagnetic dampers with a strength controlled by the input electric power. The dynamic tests started with two dampers, one on each side of the wind tunnel, introducing damping only in the heaving degree of freedom. To reach a higher damping level and suppress the resonance in the pitching degree of freedom, the system was extended including four dampers in the last three aeroelastic test cases. The amplitude of pitching motion was always kept below 0.05°. The linearity of two- and four-damper systems was successfully checked through free-decay records after releasing the model from a given out-of-equilibrium position. To minimize the contribution of still air, all the reported damping values ζ_0 in Table 2 and Table 3 were estimated from free-decaying records with an amplitude lower than 1 mm, as suggested in [2].

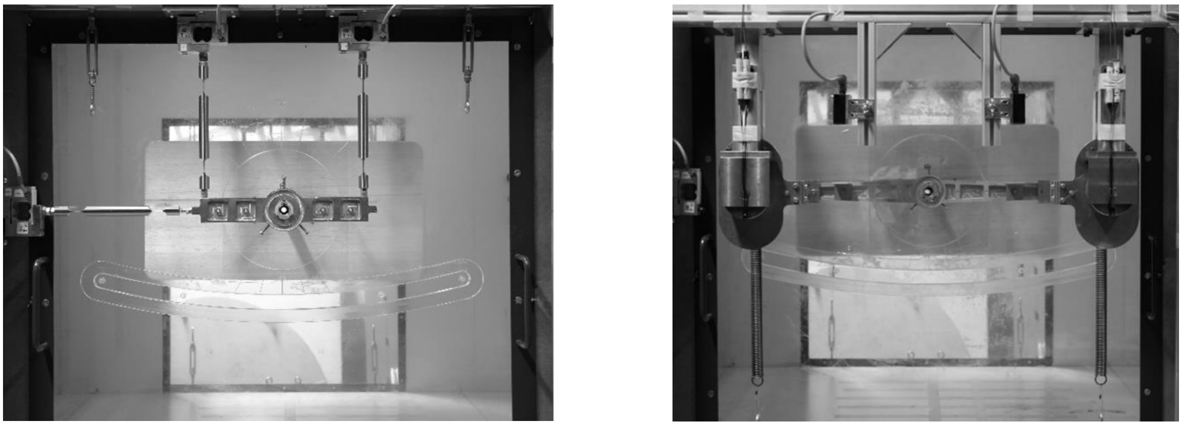

Figure 2. Photos of the static setup (left) and the aeroelastic setup with four dampers (right)

2.3 Characteristics of turbulent flow

Nominally homogeneous isotropic turbulent flow was generated by means of bi-planar wooden grid variably distanced upstream of the model (see Figure 1 (c)). The utilized gird features a mesh of 100 mm ×100 mm with 23 mm wide slats. The characteristics of the generated turbulence at the position of the model were determined through measurements at a sampling frequency of 2000 Hz with a three-component TFI Cobra probe (type 315) connecting to a NI PXI – 6259 data acquisition modulus. The measurements of flow characteristics were conducted prior to the installation of the wind tunnel model. 15 points at the position of model and 9 different mean wind speeds, ranging from 1.4m/s to 15m/s, were examined to have more knowledge about the produced turbulence with respect to its spatial distribution and its dependence on the mean flow velocity. The spatial location of the 15 checking points can be viewed in Figure 3 (b) and all the recorded signals were filtered by a digital zero-phase low-pass filter with a cut-off frequency setting at 500Hz.

The longitudinal integral length of turbulence was calculated according to Taylor's frozen-eddy hypothesis. The obtained results were checked by comparing the measured power spectrum with the well-known Von Kármán spectrum, employing the calculated integral length L_u [7]-[9]. An example of this comparison was given in Figure 3 (a).

When the mean flow velocity in the wind tunnel is higher than 4.65m/s, the turbulence characteristics like intensity and integral length get quite stable and the homogeneity of the flow also becomes good. As an example, Figure 3 (b) shows the distribution of the longitudinal turbulence intensity among the 15 checking-points. Considering that the main wind tunnel test was mainly conducted with a wind speed ranging from 5m/s to 15m/s, the spatial averaged turbulence characteristics were further averaged for wind speeds higher than 4.65m/s. Then the nominal indicators of turbulence characteristics were finally reported in Table 1 for three configurations of the turbulence grid. The obtained value is generally in parallel with the estimation of the empirical formula proposed by Roach [10] and the measurement results of a quite similar grid reported in [11]. One can also notice that the ratios of the other two turbulence intensity to the longitudinal one is lower than 1.0, implying the generated turbulence is not fully isotropic but quite close to.

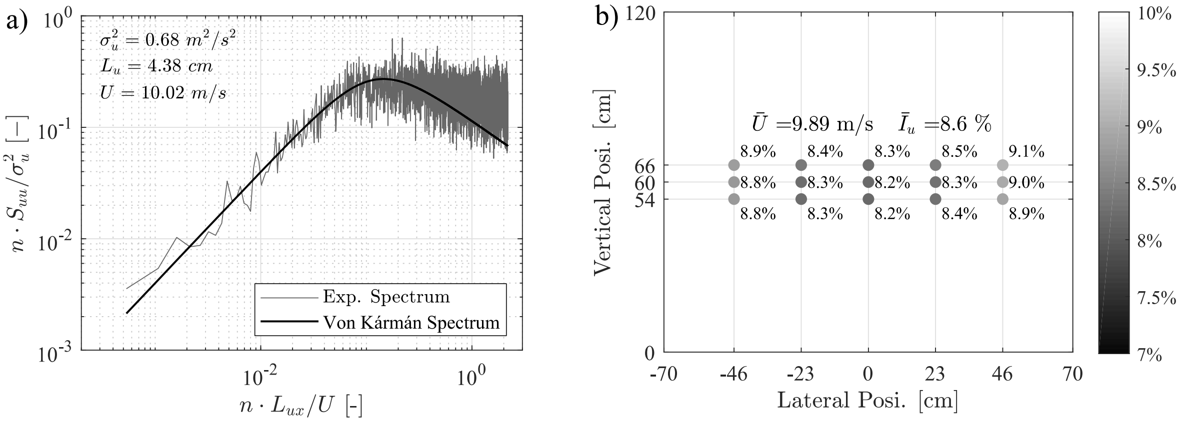

Figure 3. Examples of the characteristics of the generated turbulence with configuration “GridX94”: a) normalized power spectral densities of longitudinal turbulence fluctuations of the central checking point; b) distribution of the turbulence intensity among the 15 checking points at the position where the wind tunnel model will be installed.

Config.	x [m]	x/c [-]	I_u [-]	I_v / I_u [-]	I_w / I_u [-]	L_u [cm]	L_u / d [-]
No grid	-	-	~ 1%	-	-	-	-
GridX94	0.94	40.87	8.7%	0.82	0.85	4.41	0.74
GridX74	0.74	32.17	10.5%	0.82	0.86	3.69	0.62
GridX54	0.54	24.47	13.9%	0.82	0.88	3.10	0.52

Table 1. Characteristics of the gird-generated turbulence flow. x is the distance between the grid and the axis of model, and c is the width of the grid slat. I_u, I_v and I_w denote respectively the longitudinal, lateral and vertical turbulence intensity. L_u is the longitudinal turbulence integral length and d is the cross-wind dimensional of the bridge deck model.

3. Results in smooth flow

3.1 Static results

Combined with the sketch shown in Figure 4, the drag and lift coefficient are defined as $C_D = D/(0.5\rho U^2 d l_e)$ and $C_L = L/(0.5\rho U^2 d l_e)$, being D and L respectively the mean drag and lift over records of 100 s. The Strouhal number $St = n_{st}d/U$ is identified with the dominant Strouhal frequency peak n_{st} in the power spectral density of the fluctuating lift. $C_{lat,0}$ denotes the root-mean-square (RMS) value of fluctuating lift coefficient due to vortex shedding, obtained by integrating the same spectrum with a narrow band around n_{st}, then square-rooting and normalizing with $0.5\rho U^2 d l_e$. The Reynolds number is defined here as $Re = \rho U d/\mu$, being μ the dynamic viscosity of air.

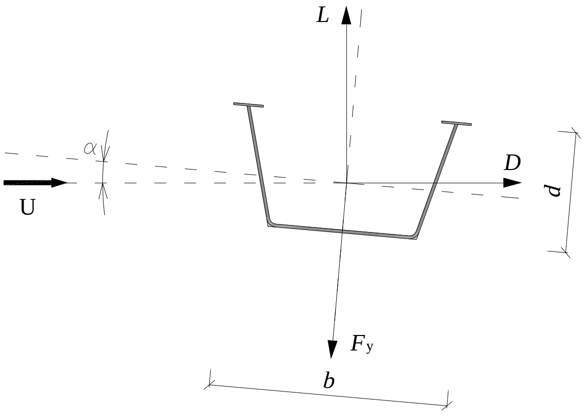

Figure 4. Definition of the aerodynamic force acting on the bridge deck model. $\alpha > 0°$ denotes a nose-up rotation of the bridge deck model and the force center was assumed at the centroid of the cross section, which is about 25mm to the bottom edge.

The 2:1 rectangular cylinder was tested first. For a null wind angle of attack, a drag coefficient between 1.50 and 1.52 and $St = 0.079$ were obtained for Re in the range $2.0 \cdot 10^4$ to $6.0 \cdot 10^4$, which well agree with the experimental results of Brooks [12] and Santosham [13]. The variation of C_D and C_L with the angle of attack α also matches the literature results in the tested range between -16° and +16°. This confirms the validity of the test setup and the end-plates. Static tests were subsequently carried out for the bridge deck model, and the main results are reported in Figure 5. The static results concerning the vortex shedding process are reported here for a lower *Re*, which is closer to the one where the VIV occurs in the later aeroelastic tests, as indicated in Table 2. For a null wind angle of attack, a drag coefficient $C_D = 1.62$ and a lift coefficient $C_L = 1.41$ are obtained for $Re = 6.0 \cdot 10^4$. In particular, the lift coefficient for this bridge deck is positive (upward) for a wide range of angles of attack roughly from -15° to 9°. In addition, the negative slope of C_L is quite clear for $-5° < \alpha < 12°$, implying the possibility of galloping instability. The galloping factor A_1, according to Den-Hartog criterion, is reported in Table 2 for five wind angles of attack around null. The static test results was found only limitedly dependent on the *Re*, except for the $C_{Lat,0}$ coefficient. As indicated in Figure 5(b), the dependence of $C_{Lat,0}$ on *Re* is especially apparent around $\alpha = 4°$, which also corresponds to a local maximum value of $C_{Lat,0}$ for the tested flow incidences. The dependence of the vortex shedding force coefficient on *Re* was also highlighted for a 3:2 rectangular cylinder in a smooth flow [3].

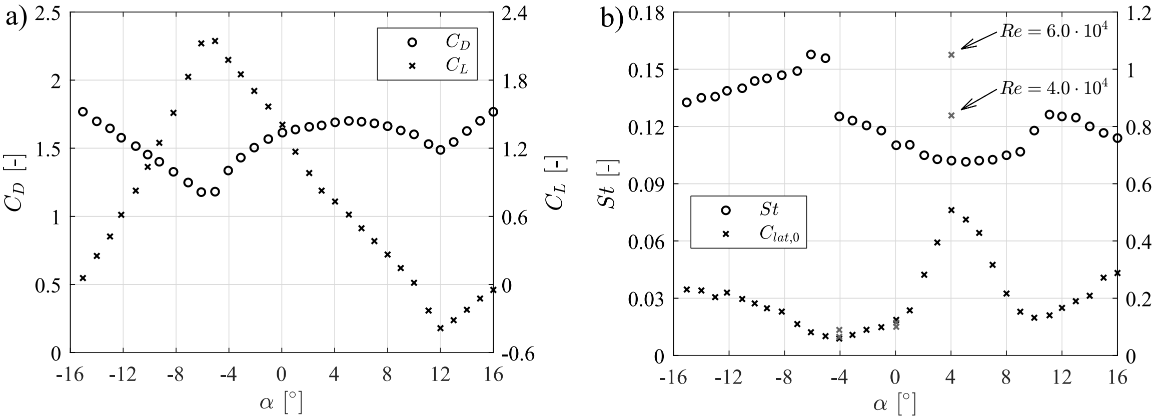

Figure 5. a) C_D and C_L at $Re = 6.0 \cdot 10^4$; b) *St* and $C_{Lat,0}$ at $Re = 2.0 \cdot 10^4$.

3.2 Aeroelastic results

The dynamic tests carried out in smooth flow are summarized in Table 2. The first five test cases investigated the effect of flow incidence α_0 considering only a low *Sc*. The other test cases focused on the behavior of the bridge deck model at $\alpha_0 = 4°$, with the *Sc* widely varied through the dampers.

Figure 6 (a) shows the effect of flow incidence α_0 on the dynamic response of the bridge deck. The galloping onset U_g predicted by the quasi-steady theory is lower than the Kármán-vortex-resonance wind speed U_r for all of the investigated α_0. In the case of $\alpha_0 = 4°$ or 2°, galloping oscillation occurs at U_r, as is typical for the combined instability of VIV and galloping [2]. For $\alpha_0 = 0°$, the instability appears neither at U_r nor at the threshold U_g predicted by the quasi-steady theory, but clearly slightly after U_r. For $\alpha_0 = -2°$, the delay beyond U_r is much more pronounced. Interestingly, a similar behavior has already been observed for a 3:2 rectangular cylinder in turbulent flow [11]. No galloping-type oscillation has been observed in the investigated wind speed range for a flow incidence of $\alpha_0 = -4°$. Figure 5 (d) shows that the magnitude of the vortex shedding force coefficient $C_{Lat,0}$ is significantly smaller for the test cases #1 to 3.

#	α_0 [deg]	St [-]	A_1 [-]	M [kg]	ρ [kg/m^3]	n_0 [Hz]	ζ_0 [%]	Sc [-]	U_r [m/s]	$Re_r \times 10^{-4}$ [-]	U_g/U_r [-]
1	-4	0.125	7.28	3.60	1.20	9.63	0.076	6.1	4.62	1.8	0.21
2	-2	0.121	6.30	3.60	1.19	9.63	0.079	6.4	4.78	1.9	0.25
3	0	0.109	9.43	3.60	1.17	9.63	0.083	6.9	5.30	2.1	0.16
4	2	0.105	8.25	3.60	1.20	9.63	0.074	6.0	5.50	2.2	0.15
5	4	0.102	4.17	3.60	1.19	9.63	0.067	5.5	5.66	2.3	0.27
6	4	0.102	4.17	3.60	1.18	9.63	0.163	13.3	5.66	2.3	0.65
7	4	0.102	4.17	3.60	1.18	9.63	0.270	22.1	5.66	2.3	1.08
8	4	0.102	4.17	3.60	1.17	9.63	0.470	38.7	5.66	2.3	1.89
9	4	0.102	4.17	3.60	1.19	9.63	0.617	50.3	5.66	2.3	2.46
10	4	0.102	4.17	3.60	1.16	9.63	0.837	69.6	5.66	2.3	3.40
11	4	0.102	4.17	3.67	1.17	9.53	0.983	83.0	5.61	2.2	4.06
12	4	0.102	4.17	3.67	1.16	9.53	1.253	106.4	5.61	2.2	5.21
13	4	0.102	4.17	3.67	1.18	9.53	1.387	115.8	5.61	2.2	5.67

Table 2. Characteristics of the aeroelastic tests for the bridge model. α_0 indicates the mean flow incidence. St denotes the Strouhal number, with the value of static tests at $Re = 2.0 \cdot 10^4$ reported. The galloping factor $A_1 = -dC_L/d\alpha(\alpha_0) - C_D(\alpha_0)$ is evaluated between $\alpha_0 - 1°$ and $\alpha_0 + 1°$. M is the effective oscillating mass, slightly depending on the number of dampers used, n_0 the natural frequency of the model in still air, $Sc = 4\pi M\zeta_0/\rho d^2 l_e$ the Scruton number, $U_r = n_0 d/St$ the Kármán-vortex resonance wind speed, $Re_r = \rho U_r d/\mu$ the Reynolds number at U_r, $U_g = 2Sc\, n_0 d\,/A_1$ the QS galloping onset, and $U_g/U_r = 2ScSt/A_1$.

Figure 6(b) shows the effect of Sc on the aeroelastic response at $\alpha_0 = 4°$. Test cases #5 to #10 show a full interaction of VIV and galloping [2], featuring the actual galloping onset wind speed fixed at V_r for Sc up to at least 69.6. Within the reduced wind speed range $V_r < V < 3.1$ ($\sqrt{2}y_{rms}/d < 0.24$), the amplitude-velocity curves do not show any significant difference with the change of Scruton number. The discrepancy becomes clear again when the reduced wind speed is higher than this range. A similar behavior was also observed for a 3:2 and a 1:2 rectangular cylinder undergoing full interaction of VIV and galloping [3][14]. For $Sc \geq 83$, VIV and galloping begin to separate and a clear velocity-restricted VIV range appears after V_r. It is interesting to note that test cases #11 to #13 preserve the same slope of the amplitude-velocity curve as that of tests #5 to #10 in the lock-in range. The galloping onset speed was intentionally not reached for test cases #11 to #13 not to risk to destroy the model. Nevertheless, a higher amplitude branch was found beyond the lock-in wind speed range by releasing the model from a given displaced position. Finally, it is worth noting here that a typical value of Sc for this kind of bridge deck in the launching phase ranges from 10 to 30.

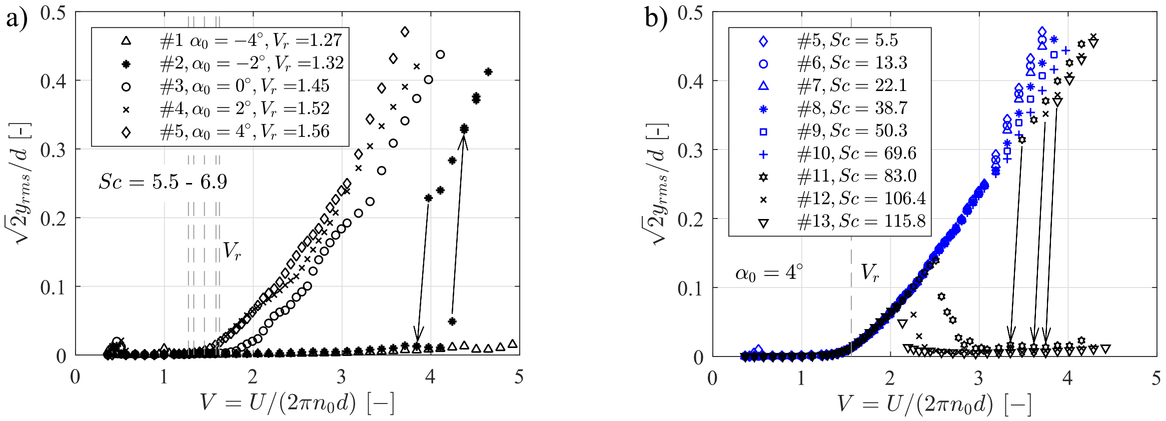

Figure 6. Dynamic response of the bridge deck model: a) effect of the flow incidence α_0; b) effect of the Scruton number Sc at $\alpha_0 = 4°$. y_{rms} represents the RMS value of the displacement response y.

In the velocity range $V_r < V < 3.1$, the vibration time histories of the model exhibit the amplitude modulation phenomenon (observed also in [2] [3]), even for test cases #11 to 13, as exemplified by the records reported in Figure 7(a) and (b). Despite the fact that the equivalent amplitude $\sqrt{2}y_{rms}/d$ is nearly the same, test case #5, featuring a lower Sc, shows quicker variation of the amplitude compared to test case #10 for the same V (Figure 7(a) and (b)). For test cases #5 to #10, the time-amplitude of vibration becomes nearly constant for wind speeds higher than about 3.1. The power spectral density of the displacement response for test case #5 at $V/V_r = 1.32$ is provided in Figure 7(c), which shows a pitchfork shape around the natural frequency n_0. This pitchfork is only visible when the amplitude modulation phenomenon occurs. Finally, it is worth noting that the Strouhal frequency $n_{st} = StU/d$ can no longer be detected in the spectra for test cases #5 to #10 (full interaction of VIV and galloping) once the reduced wind speed is higher than V_r.

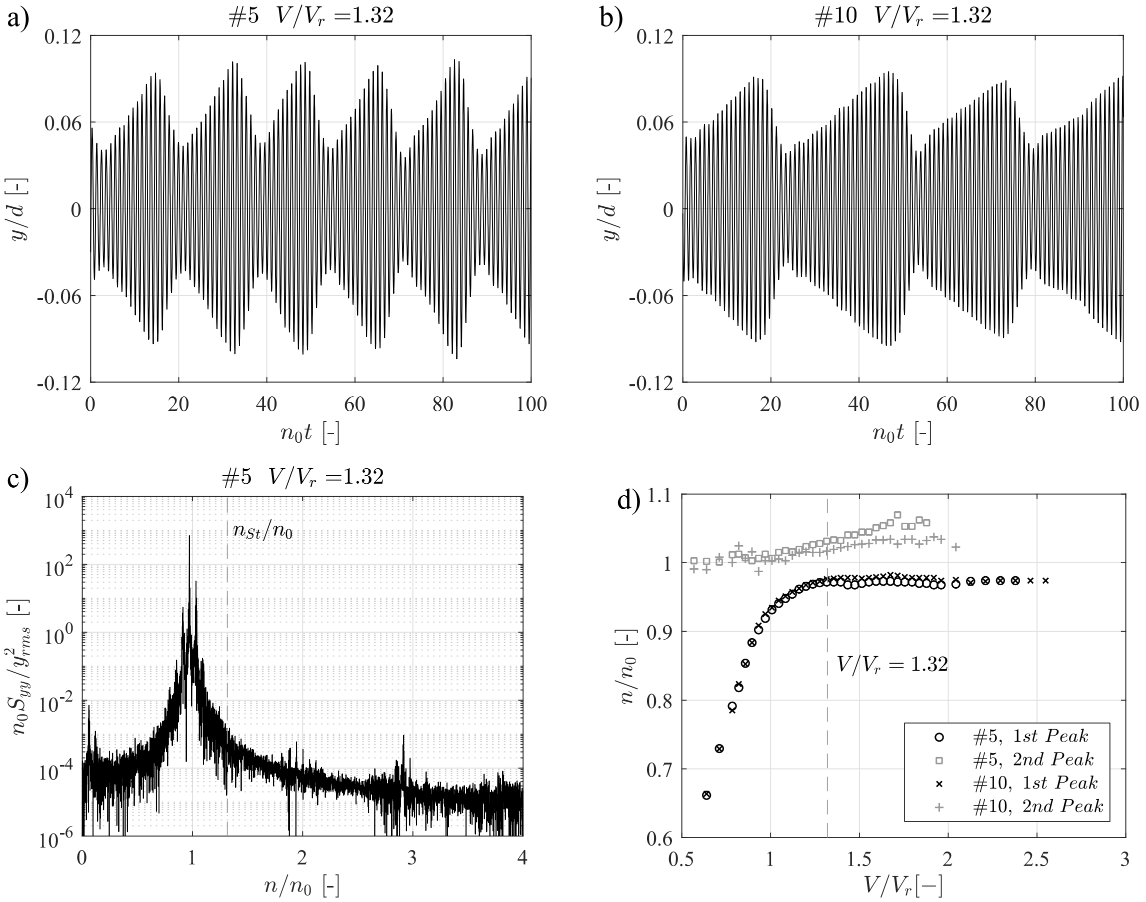

Figure 7. a) - b) time records for test cases #5 and #10 at V/V_r =1.32; c) normalized power spectral density of displacement response y for test case #5 at V/V_r =1.32; d) collected frequency peaks at various wind speeds for test cases #5 and #10, being '1st peak' the dominant peak in the spectrum and '2nd peak' the second strongest peak.

Figure 7(d) collects the frequency peaks from the power spectral density of displacement response for test cases # 5 and #10, at various wind speeds. The term '1st peak' denotes the dominant peak in the spectrum, while '2nd peak' is the second strongest peak. With the increase of V, the vortex shedding frequency, which is the 1st peak and follows the Strouhal law before V_r, gradually evolves into the model's main oscillating frequency, with a value slightly lower than n_0. On the other hand, the natural frequency n_0, which roughly corresponds to the 2nd peak before V_r, gradually becomes the right-side peak of the spectral pitchfork during amplitude modulation phenomenon with a value higher than n_0. After amplitude modulations disappear at higher V, the '2nd peak' becomes the first superharmonic of the '1st peak', and it is not included in the plot. This evolution in the frequency domain was also reported for a 2:1 rectangular cylinder by Itoh & Tamura [14].

Slight but clear differences can be observed between test cases #5 and #10. In particular, test case #10 features a slightly higher oscillating frequency (1st peak) than test case #5 in the wind speed range where the amplitude modulation phenomenon is observed. There, the 2nd peak of test case #10 is located closer to the 1st peak, and this smaller frequency gap is consistent with the longer period of amplitude modulation (Figure 7(b)). Beyond this range, their 1st peaks present nearly the same values.

4. Effect of the presence of turbulence

For most of the time, realistic bridges are immersed in a turbulent flow. Although Parkinson and co-workers [15] have shown that it is the turbulence intensity mainly makes a difference to the galloping instability of bluff body, a recent experimental work points out that the turbulence integral length plays also a very important role [11]. Nevertheless, the first stage of this research work regards to a turbulent flow with a medium-high intensity and an integral length in the same order of the cross dimension of the bridge deck model.

4.1 On the static results

Figure 8 shows the results obtained from the static test in turbulent flow, including also the results in smooth flow for a sake of comparison. In turbulent flow, the drag coefficient was found decreased around the null wind angle of attack and the range of flow incidence featuring a negative slope of lift coefficient also becomes narrower. However, the galloping factors for this bridge deck increases for some interesting wind angle of attack in turbulent flow (see the galloping factor A_1 in Table 2 for smooth flow and that in Table 3 for turbulent flow). In particular, all the investigated turbulent flow promoted a higher galloping factor for the 4° wind angle of attack, increasing from 4.2 in smoth flow to 7.9, 6.9 and 5.2 in turbulent flow. A decrease of Strouhal number was also found in turbulent flow, which is particularly visible for a flow incidence ranging from -4° to 8°. For these three kinds of generated turbulence flows, the value of *St* seems not affected too much by the turbulence intensity. The unsteady lift coefficient $C_{lat,0}$ in turbulent flow was also reported here, adopting the same method as previously mentioned except that a wider frequency-band was used to integrated the power spectral density of lift around the Strouhal frequency peak f_{st}. Since the turbulence can also contribute to a part of unsteady lift acting on the model, the coefficient $C_{lat,0}$ was found a little higher in turbulent flow for the flow incidence outside 0° to 8°. But around 4° flow incidence, it is clear that the strong vortex shedding force in smooth flow was suppressed by turbulence. Anyway, a local maximum of $C_{lat,0}$ was still kept around 4° in turbulent flow except that for the higher turbulence intensity I_u =13.9%.

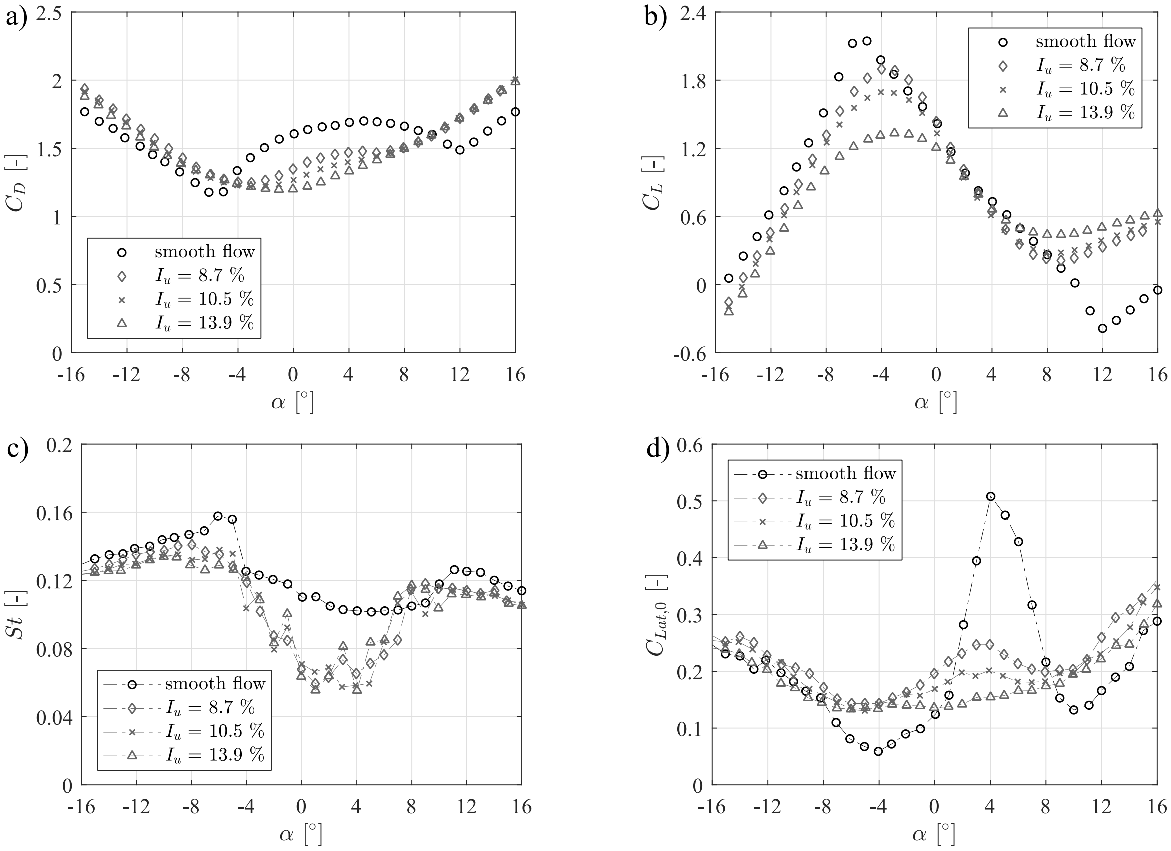

Figure 8. Static test results in turbulent flow: a) -b) the mean drag and lift coefficient at *Re* = 6.0·10^4; c)- d) the Strouhal number and the strength of vortex shedding force at *Re* = 2.0·10^4

4.2 On the aeroelastic behavior

The dynamic tests carried out in turbulent flow are listed in Table 3. The first four test cases represent an investigation of the effect of flow incidence with a low Sc number considered. Test case #T4 to #T12 studied the effect of Scruton number for the flow incidence of 4°. While the above test cases are all carried out in turbulent flow with an intensity of 8.7%, the last two test cases checked the effect of turbulent flow with higher intensity, particularly focusing on the 4° flow incidence with a low Scruton number considered.

For a low Sc number, it can be found that the galloping instability of this bridge deck still rises firstly at a flow incidence of 4° in turbulent flow (see Figure 9 a)). This “most disadvantageous” flow incidence corresponds well to the position of the local maximum of $C_{\mathrm{lat},0}$ - α curve that reported in Figure 8 d). It is necessary to state that such a phenomenon was also observed for turbulent flows with higher intensity (I_{u} = 10.5% and 13.9%), although they are not reported here for the sake of brevity. Combining the results obtained in smooth flow(see Figure 6 (a)), it seems reasonable to suggest that the presence of turbulence will not change the “most disadvantage” flow incidence of this bridge deck when a low Sc number is discussed. And it also implies that the position of the local maximum of $C_{\mathrm{lat},0}$ could be a more useful indicator for the “most disadvantageous” flow incidence in this case, rather than the galloping factor A_1.

#	I_u [%]	α_0 [deg]	St [-]	A_1 [-]	M [kg]	ρ [kg/m^3]	n_0 [Hz]	ζ_0 [%]	Sc [-]	U_r [m/s]	$Re_r \times 10^{-4}$ [-]	U_g/U_r [-]
T1	8.7	-2	0.087	5.41	3.89	1.20	6.94	0.035	3.0	4.79	1.91	0.10
T2	8.7	0	0.068	10.98	3.89	1.19	6.94	0.033	2.9	6.12	2.45	0.04
T3	8.7	2	0.063	9.87	3.89	1.20	6.94	0.036	3.1	6.61	2.64	0.04
T4	8.7	4	0.065	7.86	3.89	1.22	6.94	0.038	3.2	6.41	2.56	0.05
T5	8.7	4	0.065	7.86	3.89	1.22	6.94	0.124	10.6	6.41	2.56	0.18
T6	8.7	4	0.065	7.86	3.89	1.21	6.94	0.269	23.3	6.41	2.56	0.39
T7	8.7	4	0.065	7.86	3.89	1.22	6.94	0.429	36.8	6.41	2.56	0.61
T8	8.7	4	0.065	7.86	3.89	1.21	6.94	0.590	51.2	6.41	2.56	0.85
T9	8.7	4	0.065	7.86	3.89	1.21	6.94	0.822	71.1	6.41	2.56	1.18
T10	8.7	4	0.065	7.86	3.89	1.21	6.94	1.083	93.7	6.41	2.56	1.55
T11	8.7	4	0.065	7.86	3.89	1.20	6.94	1.405	122.8	6.41	2.56	2.03
T12	8.7	4	0.065	7.86	3.89	1.21	6.94	1.652	143.3	6.41	2.56	2.37
T13	10.5	4	0.059	6.86	3.77	1.18	6.22	0.041	3.5	6.33	2.53	0.06
T14	13.9	4	0.055	5.18	3.76	1.20	5.14	0.046	3.9	5.61	2.24	0.08

Table 3. Characteristics of the aeroelastic tests for the bridge model in turbulent flow. I_u denotes the longitudinal turbulence intensity, see also the caption of Table 2.

On the other hand, one may also notice that all of the observed galloping thresholds reported in Figure 9 (a) are higher than the critical wind speed for vortex resonance U_r. While the strong interaction between VIV and galloping in smooth flow is able to promote an unsteady galloping arising at the U_r for a flow incidence of 4°, such a feature was not kept in turbulent flow with an intensity $I_u \geq 8.7\%$ (see also Figure 10). Figure 9 (b) further shows the effect of varying Scruton number in turbulent flow, for the wind angle of attack of 4°. Differing from the behavior in smooth flow, the galloping onset in turbulent flow right now increases with the increase of Scruton number. From a low to medium-high Scruton number, the amplitude-velocity slope can be also found decreased with the increase of Sc number. Such a difference of amplitude-slope can only be observed for $\sqrt{2}y_{\mathrm{rms}}/d > 0.25$ in smooth flow (see Figure 6 (b), Sc =5.5~69.6). It should be also mentioned that the complex amplitude modulation phenomenon was not observed anymore in turbulent flow. For a higher Scruton number, like Sc = 116~123, the galloping onset in smooth has not been reached until a reduced wind speed of V = 4.5 (Test case #13, Sc =115.8) but it already occurs around V = 4 in turbulent flow with I_u = 8.7% (Test case #T11, Sc =122.8). This qualitatively confirms the previously mentioned increase of galloping factor A_1 in turbulent flow.

Figure 10 shows that effect of turbulence intensity on the galloping behavior of this bridge deck, at the 4° flow incidence with a very low Sc considered. The results in smooth flow were also replotted here for a comparison. The existence of turbulence and the increase of turbulence intensity was found able to postpone the threshold of galloping instability. Again, how much the galloping onset is delayed behind the U_r seems to hold a relationship with the strength of $C_{\mathrm{lat},0}$ (see Figure 8(d)). Another feature should be noticed is, that the amplitude of galloping oscillation increases faster in turbulent flow after the galloping onset is reached.

Finally, it must be stated here that a self-limited primary Kármán-vortex induced vibration has not been observed during the whole aeroelastic tests in turbulent flow.

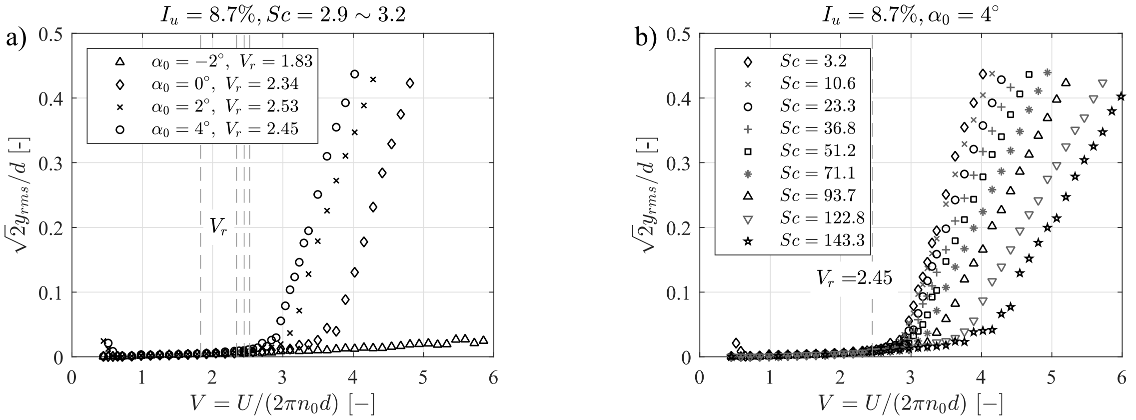

Figure 9. Dynamic response in turbulent flow with an intensity of I_u = 8.7%: a) the effect of wind angle of attack in case of a low Scruton number; b) the effect of Scruton number for wind angle of attack of 4°. See also the caption of the Figure 6.

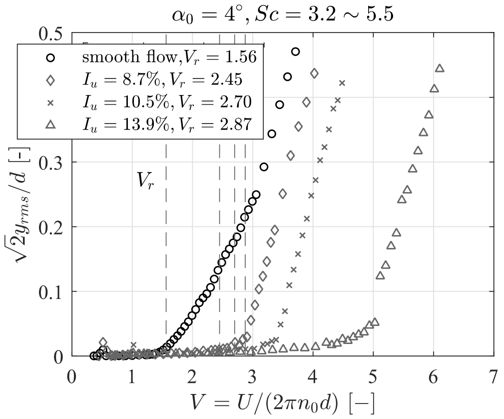

Figure 10. Dynamic response in turbulent flow with various turbulence intensity. See also the caption of the Figure 6.

5. Concluding remarks

Wind tunnel tests showed that the studied bridge deck is prone to the unsteady galloping instability which occurs at low reduced wind speeds, given that a low Scruton number is expected during the launching phase of steel-concrete composite bridges. The sensitivity of the unsteady galloping instability to the flow incidence is highlighted for the considered geometry.

In a smooth flow, strong interaction between VIV and galloping was observed at 4° flow incidence, with the galloping onset being fixed at the Kármán-vortex-resonance wind speed up to a Scruton number of at least 70. In contrast, for the 0° flow incidence, the galloping instability arises at a flow speed higher than the vortex-resonance one, even for a very low value of the mass-damping parameter. Static tests suggest that the very different magnitude of the vortex shedding force at different flow incidences might play a role in this behavior.

In a turbulent flow with I_u = 8.7% - 13.9%, the "most disadvantageous" flow incidence for the unsteady galloping instability of this bridge deck was found still kept at 4° flow incidence, in case of a low Scruton number involved. And it is interesting that the 4° flow incidence also corresponds to a local maximum of the vortex shedding force strength as indicated by the static tests in turbulent flow. However, very different from the phenomenon in a smooth flow, the galloping instability at 4° flow incidence was found always arising at a flow velocity higher than the Kármán-vortex-resonance wind speed. Either the galloping onset can not be fixed at one position anymore when the Scruton number was varied in small steps. Finally, an increase of the turbulence intensity was found able to further postpone the unsteady galloping onset.

6. Literatur

[1] G.V. Parkinson and N.P.H. Brooks, On the aeroelastic instability of bluff cylinders, J. Appl. Mech., 28 (1961) 252-258.

[2] C. Mannini, A.M. Marra and G. Bartoli, VIV-galloping instability of rectangular cylinders: review and new experiments, J. Wind Eng. Ind. Aerod., 132 (2014) 109-124.

[3] C. Mannini, A.M. Marra, T. Massai and G. Bartoli, Interference of vortex-induced vibration and transverse galloping for a rectangular cylinder, J. Fluids Struct., 66 (2016) 403-423.

[4] EN 1991-1-4, Eurocode1-Actions on Structures-Parts 1-4: General Actions -Wind Actions, 2010.

[5] S. O, Hansen, Wind loading design codes, Fifty Years of Wind Engineering-Prestige Lectures from the Sixth European and African Conference on Wind Engineering, UK, 2013, pp. 35-68.

[6] G. Hanswille. Anwendung der Teile 2 der Eurocodes 3 und 4 für Stahl-und Verbundbrücken: Erste Erfahrungen und europäische Überlegungen zur Weiterentwicklung der Regelwerke, Stahlbau, 83 (2014) 217-226 (in German).

[7] T. von Kármán, Progress in the statistical theory of turbulence, Proc. Natl. Acad. Sci. 34(1948), 530–539.

[8] M. Clobes, Identifikation und Simulation instationärer übertragung der Windturbulenz im Zeitbereich, Shaker, 2008.

[9] T. Höbbel, K. Thiele and M. Clobes, Wind turbulence parameters from three dimensional full-scale measurements at 344 m high guyed mast site Gartow 2, J. Wind Eng. Ind. Aerod.172 (2018) 341-350.

[10] P. E. Roach, The generation of nearly isotropic turbulence by means of grids, International Journal of Heat and Fluid Flow, 8(1987) 82-92.

[11] C. Mannini, T. Massai and A.M. Marra, Unsteady galloping of a rectangular cylinder in turbulent flow, J. Wind Eng. Ind. Aerod., 173 (2018) 210-226.

[12] P.N.H. Brooks, Experimental investigation of the aeroelastic instability of bluff two-dimensional cylinders, M.Sc. thesis, Vancouver, Canada, University of British Columbia, 1960.

[13] T.V. Santosham, Force measurements on bluff cylinders and aeroelastic galloping of a rectangular cylinder, M.Sc. thesis, Vancouver, Canada, University of British Columbia, 1966.

[14] Y. Itoh and T. Tamura, The role of separated shear layers in unstable oscillations of a rectangular cylinder around a resonant velocity, J. Wind Eng. Ind. Aerod., 90 (2002) 377-394.

[15] A. Laneville and G.V. Parkinson, Effects of turbulence on galloping of bluff cylinders, Proceedings of the 3rd International Conference on Wind Effects on Buildings and Structures, Tokyo, Japan, Saikon, Co. Ltd., 1971, pp.787-797.